Supplementary Information

Effect of R-site Element on Crystalline Phase and Thermal Stability of Fe Substituted Mn Mullite-type Oxides: $R_2(Mn_{1-x}Fe_x)_4O_{10-\delta}$ (R = Y, Sm or Bi; x = 0, 0.5, 1)

Sampreetha Thampy,[a] Nickolas Ashburn,[a] Thomas J. Martin,[b] Chenzhe Li,[c] Yongping Zheng,[a] Julia Y. Chan,[b] Kyeongjae Cho,[a] and Julia W. P Hsu[a*]

[a]Department of Materials Science and Engineering, University of Texas at Dallas, Richardson, TX 75080, USA

[b]Department of Chemistry and Biochemistry, University of Texas at Dallas, Richardson, TX 75080, USA

[c]School of Mechanical and Aerospace Engineering, Seoul National University, Seoul 151-742, Republic of Korea

* Corresponding author: Department of Materials Science and Engineering, University of Texas at Dallas, Richardson, Texas 75080, USA; Phone: +1 (972) 883-5789
E-mail: jwhsu@utdallas.edu

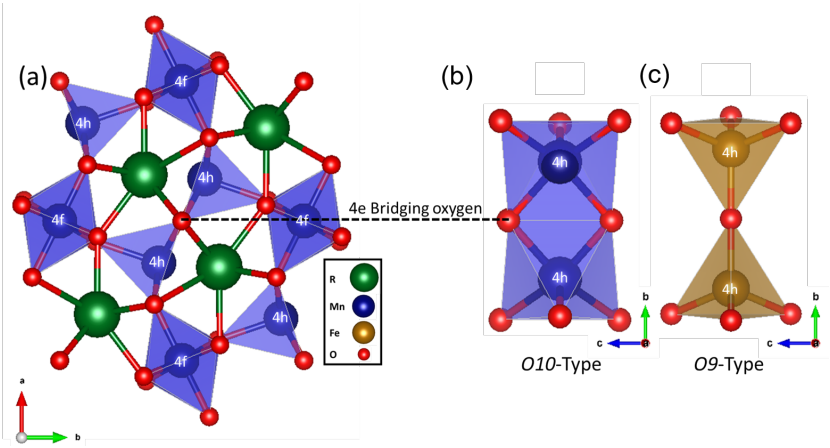

Fig. S1. (a) Crystal structure of mullite-type oxides. Atoms are labeled with their Wyckoff symbols. (b) Edge-shared MO_5 square pyramids in *O10*-type structure. (c) Vertex-sharing MO_4 tetrahedral in *O9*-type structure. Green, blue, brown, and red balls represent R, Mn, Fe, and O atoms, respectively.

Table S1. U values used in this work for oxide systems and the energy adjustments between previous work and this work.

Element	U_{eff} (eV)	ΔE_M(eV)	ΔE_M (eV)[a]
Fe	4.0	2.0	1.7
Mn	3.9	1.8	1.7

[a] Ref. 1

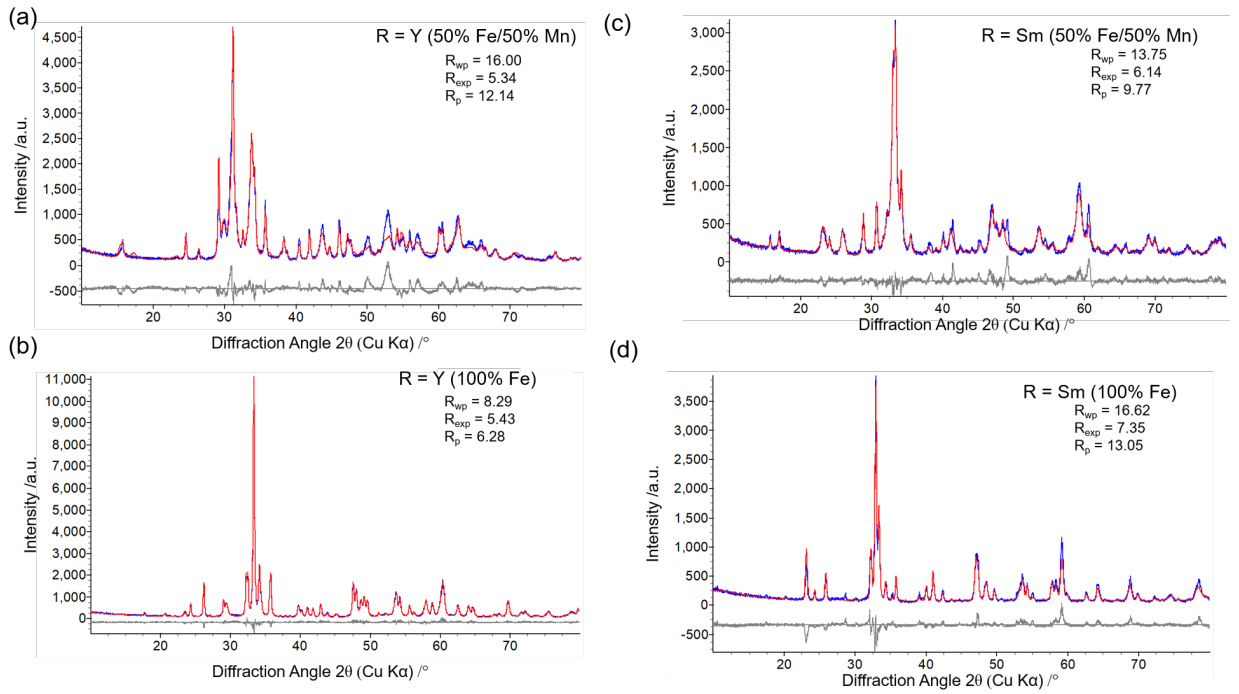

Fig. S2. Rietveld refinement plot of (a, b) R = Y; (c, d) R = Sm for 50% Fe/50% Mn and 100% Fe, respectively in the reactants. The blue, red, and grey lines represent the experimental, calculated, and difference patterns, respectively. Phase compositions and lattice parameters for the mullite-type compounds are summarized in Table S2 and S3, respectively. $\lambda_{K\alpha1}$ = 0.15406 nm wavelength was used in the refinement.

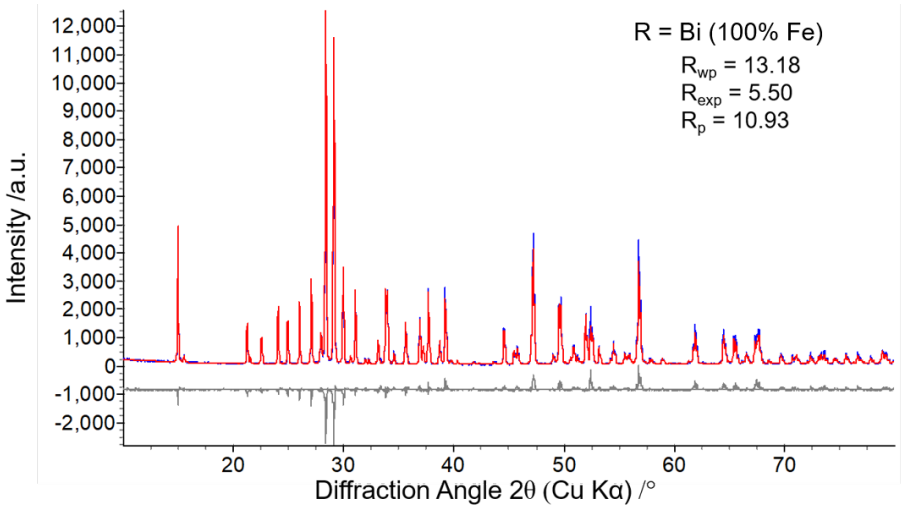

Fig. S3. Rietveld refinement plot of $Bi_2Fe_4O_9$. The blue, red, and grey lines represent the experimental, calculated, and difference patterns, respectively. Phase compositions and lattice parameters for the mullite-type compounds are summarized in Table S2 and S3, respectively. $\lambda_{K\alpha1}$ = 0.15406 nm wavelength was used in the refinement.

Table S2. Phase composition of $R_2(Mn_{1-x}Fe_x)_4O_{10-\delta}$ (R = Y, Sm, Bi)

R-site	M-site	Phase Composition	% Phase Purity
Y			
	100% Mn	$Y_2Mn_4O_{10}$	100
	50% Fe/50% Mn	$Y_2Mn_{1.88(2)}Fe_{1.87(2)}O_{10}$ $YFeO_3$ Mn_2O_3 $YMnO_3$	55.3(5) 20.9(4) 16.4(6) 7.4(1)
	100% Fe	$YFeO_3$ Fe_2O_3 $Y_3Fe_5O_{12}$ Y_2O_3	56.6(1) 27.4(1) 10.5(1) 5.5(1)
Sm			
	100% Mn	$Sm_2Mn_4O_{10}$	100
	50% Fe/50% Mn	$Sm_2Mn_{2.22(3)}Fe_{2.00(4)}O_{10}$ $SmFeO_3$ Mn_2O_3	18.2(3) 47.0(5) 34.8(5)
	100% Fe	$SmFeO_3$ Fe_2O_3	72.1(4) 27.9(4)
Bi			
	100% Mn	$Bi_2Mn_4O_{10}$	
	50% Fe/50% Mn	$Bi_2Mn_{2.23(4)}Fe_{2.00(2)}O_{10}$ $Bi_2Fe_{4.00(4)}O_9$ Mn_2O_3	54.4(4) 41.8(4) 3.8(3)
	100% Fe	$Bi_2Fe_{4.16(1)}O_9$ Bi_2O_3 $BiFeO_3$	95.1(1) 4.0(1) 0.9(1)

Table S3. Rietveld refined and simulated lattice parameters and Fe ground state occupation sites in the single unit cell for $R_2(Mn_{1-x}Fe_x)_4O_{10-\delta}$ (R = Y, Sm, Bi).

	Experimental (nm)			Theoretical (nm)			
R = Y	*a*	*b*	*c*	*a*	*b*	*c*	Fe
100% Mn [a]	0.72667(6)	0.84732(6)	0.56663(4)	0.736	0.855	0.576	-
50%Fe/50%Mn	0.72801(10)	0.84625(12)	0.56746(8)	0.733	0.860	0.577	4*h*
R = Sm	*a*	*b*	*c*	*a*	*b*	*c*	
100% Mn [a]	0.74296(4)	0.85802(5)	0.56908(3)	0.751	0.866	0.578	-
50%Fe/50%Mn	0.74190(20)	0.85680(20)	0.56837(15	0.749	0.870	0.578	4*h*
R = Bi	*a*	*b*	*c*	*a*	*b*	*c*	
100% Mn [a]	0.75652(2)	0.85370(2)	0.57635(1)	0.759	0.864	0.584	-
50%Fe/50%Mn				0.758	0.873	0.583	4*h*
O10-type	0.76066(8)	0.84996(10)	0.58019(6)				
O9-type	0.77083(9)	0.84452(11)	0.58682(6)				
100% Fe	0.79689(2)	0.84487(2)	0.60093(1)	0.808	0.855	0.610	4*f*,4*h*

[a] Ref. 1

Figure. S4 shows the density of states (DOS) for unstable $Bi_2Fe_4O_{10}$ (*O10*) and stable $Bi_2Fe_4O_9$ (*O9*) compounds with 100% Fe substitution. According to crystal field theory, Fe d-electrons in octahedral (4*f*) and polyhedral (4*h*) sites follow high spin $3d^5$ state.[2] In *O10-type* structure (Fig. S4a), the increase in Fe concentration ($x \geq 0.6$) forces Fe into the 4*f* octahedral sites resulting in significant Jahn-Teller distortion; the e_g and t_{2g} states of Fe in 4*f* octahedra show further splitting into five different recognizable states, including an empty state in the middle of the band gap (labeled as t_{2g}^* and e_g^* in Fig. S4a). This new empty state indicates an increase in the oxidation state of Fe greater than 3+, which leads to Fe instability. Moreover, the empty state results in the removal of an additional electron from the half-filled d shell along with an increase in the minority spin caused by an increase in bonded electrons. This is energetically unfavorable per Hund's Rule and Fe's strong exchange interaction[3] resulting in decreased stability of *O10*-type structure (Fig. 6). Contrary to the distorted Fe octahedral occupation in *O10*-type structures, Fe in pyramidal sites (Fig. S4b) show no clear evidence for serious Jahn-Teller distortion and therefore does not decrease the system stability. For *O9*-type structure, there is no over oxidation of Fe in the substituted octahedral (Fig. S4c) or tetrahedral sites (Fig. S4d), thus no e_g or t_{2g} states below the Fermi level. Since *O9*-type structures have 3+ octahedral and tetrahedral sites, we see stable Fe substitution into both locations resulting in a DOS similar to that found in the *O10*-type

pyramidal sites. This exchange interaction induced separation of occupied majority spin states from unoccupied minority spin states gives Fe its most stable configuration with a half-filled d-shell allowing for *O9*-type formation.

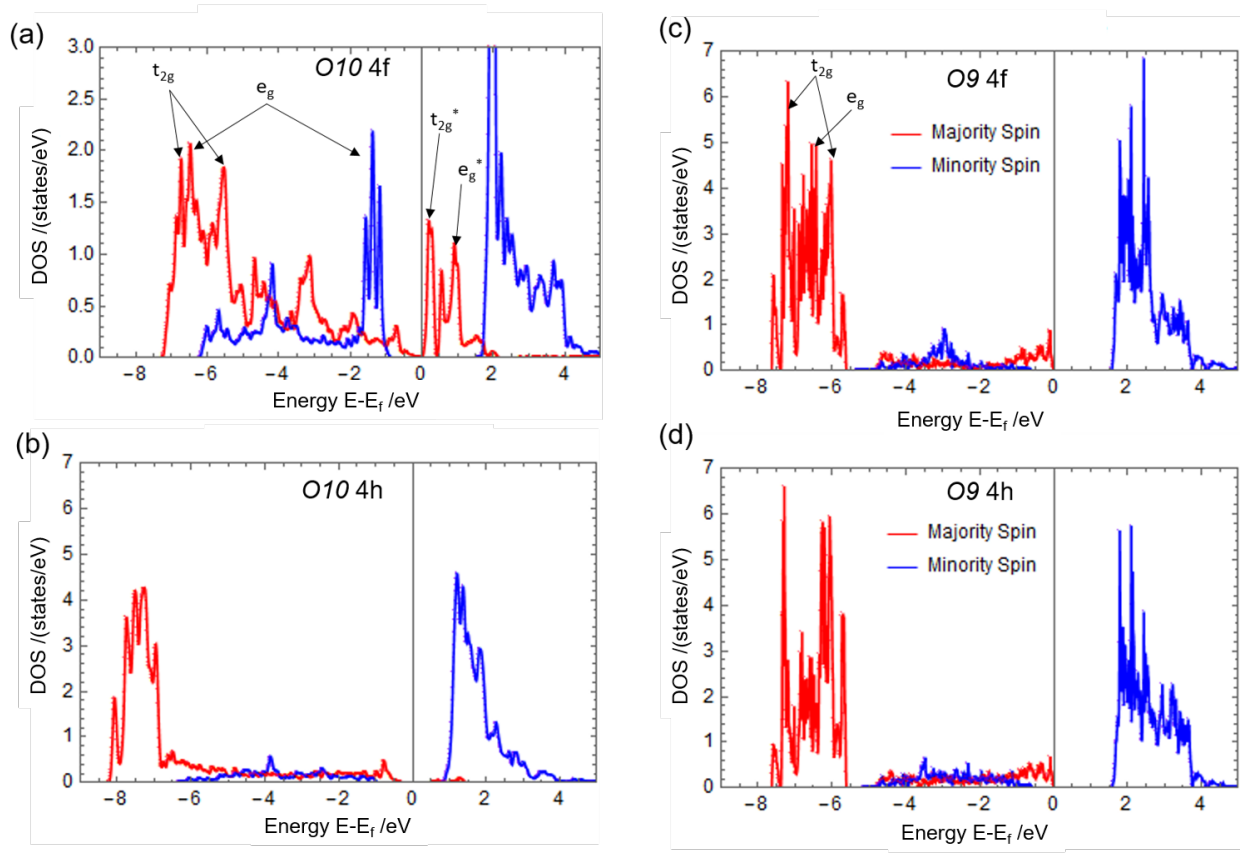

Fig. S4. Density of states for (a, b) $Bi_2Fe_4O_{10}$ (*O10*) and (c, d) $Bi_2Fe_4O_9$ (*O9*). States of Fe d-elections in (a) 4*f* octahedral and (b) 4*h* pyramid sites in $Bi_2Fe_4O_{10}$, respectively. (c) 4*f* octahedral and (d) 4*h* tetrahedral sites in $Bi_2Fe_4O_9$, respectively. Red and blue represents majority and minority spins, respectively. (*Total DOS was divided by 5 to clearly illustrate Fe p-DOS.).

In contrast to Fe, Mn compound shows a lower stability in *O9*-type structures (Fig. S5a). In $Bi_2Mn_4O_9$ *O9*-type structure, octahedral chains show high d orbital electron density right below the Fermi level (Fig. S5a, black arrow). This indicates that Mn atoms are still highly reactive. On the other hand, in *O10*-type structure DOS for the 4*f* octahedral site (Fig. S5b) shows an electron density decrease (Fig. S5b, black arrow) while the non-bonding states (Fig. S5b, green arrow) increase above Fermi level. This is due to the higher oxidation state of Mn to 4+, resulting in lower reactivity from Mn atoms and no Jahn-Teller distortion, hence a more stable structure. Because Mn^{3+} is known to have stable first order Jahn-Teller distortion,[4] having

Mn^{3+} ion in the 4*f* octahedral site of *O9*-type will destabilize the structure as Mn^{3+} would attempt to elongate the z direction. Consequently, these Mn^{3+} substituted octahedral sites exhibit small amounts of second order Jahn-Teller distortion in the a-b plane attempting to compensate for lack of first order Jahn-Teller distortion, decreasing stability of *O9*-type Mn compound. Mn^{3+} is also unstable when placed in a tetrahedral site in the *O9*-type structure; in the tetrahedral site, the formation energy is 0.8 eV lower than that of Mn substituted octahedral sites due to lack of Jahn-Teller distortion. Thus, it is difficult to form pure Mn compounds with *O9*-type structure. These results clearly show that the pure Fe compound can never form stable $Bi_2Fe_4O_{10}$ *O10*-type structure and the pure Mn compound can never form stable $Bi_2Mn_4O_9$ *O9*-type structure.

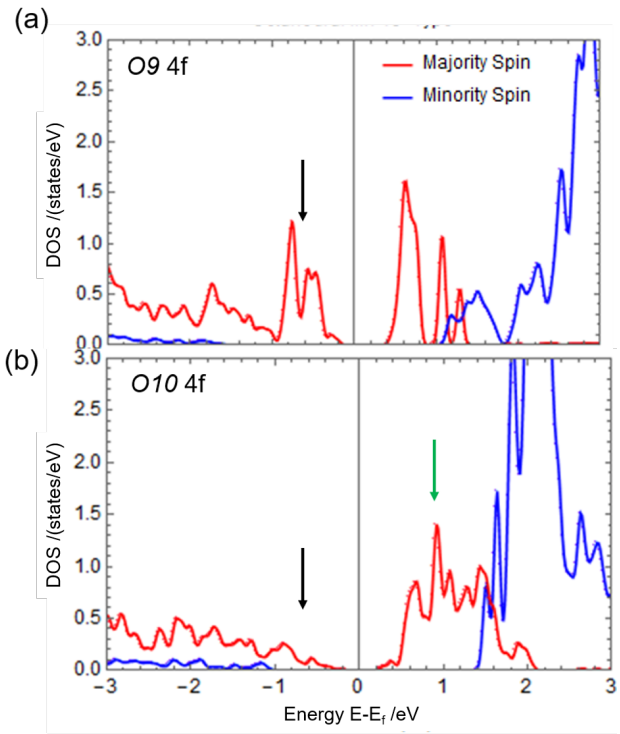

Fig. S5. Density of states for 4*f* octahedral Mn d-shell electrons in (a) $Bi_2Mn_4O_9$ *O9*-type and (b) $Bi_2Mn_4O_{10}$ *O10*-type. The black arrows show high *d* orbital electron density right below the Fermi level. The green arrow shows the formation of additional non-bonding states representing the higher oxidation state of Mn. Red and blue represents majority and minority spins, respectively.

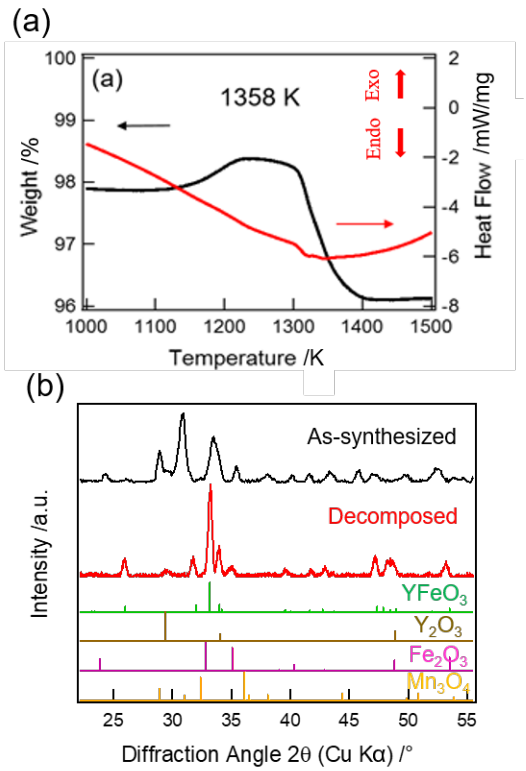

Fig. S6. (a) Zoom in view of TGA (black) and DSC (red) curves showing the decomposition region for R = Y for 50% Fe and 50% Mn in the reactants. (b) XRD pattern of as-synthesized (black) and decomposed (red) samples, respectively. Respective reference diffraction data are shown.

References

1 C. Li, S. Thampy, Y. Zheng, M. Kweun, Y. Ren, J. Y. Chan, H. Kim, Cho, M. Cho Y. Y. Kim, J. W. P. Hsu and K. Cho, J. Phys.: Condens. Matter, 2016, **28**, 125602 (pp1-10).

2 J. B. Goodenough, Ann. Rev. Mater. Sci., 1998, **28**, 1-27.

3 I. B. Bersuker. Chem. Rev., 2013, **113**, 1351-1390.

4 K. Fantai, R. C. Longo, M. S. Park, J. Yoon, D. H. Yeon, J. H. Park, W. H. Wang, K. C. Santosh, S. G. Doo and K. Cho, J. Mater. Chem. A, 2015, **3**, 8489-8500.